

The Accretion History of AGN: A Newly Defined Population of Cold Quasars

Allison Kirkpatrick 1, C. Megan Urry 2, D. Jason Brewster 4, Kevin C. Cooke 5, Michael Estrada 1, Eilat Glikman 6, Kurt Hamblin 4, Tonima Tasnim Ananna 2, D. Casey Carlile 1, Brandon Coleman 1, Jordan Johnson 1, Jeyhan S. Kartaltepe 5, Stephanie M. LaMassa 7, Stefano Marchesi 8, Meredith Powell 2, Dave Sanders 1, Dave Sanders 1, Ezequiel Treister 1, and Traceye Jan Turner 4, 12, D. Dave Sanders 1, Ezequiel Treister 1, and Traceye Jan Turner 4, 12, D. Dave Sanders 1, Ezequiel Treister 1, and Traceye Jan Turner 4, 12, D. Dave Sanders 1, Ezequiel Treister 1, and Traceye Jan Turner 4, 12, D. Dave Sanders 1, Ezequiel Treister 1, and Traceye Jan Turner 4, 12, D. Dave Sanders 1, Ezequiel Treister 1, and Traceye Jan Turner 4, 12, D. Dave Sanders 1, Ezequiel Treister 1, and Traceye Jan Turner 4, 12, D. Dave Sanders 1, Ezequiel Treister 1, and Traceye Jan Turner 4, 12, D. Dave Sanders 1, Ezequiel Treister 1, and Traceye Jan Turner 4, 12, D. Dave Sanders 1, Dave Sanders

Abstract

Quasars are the most luminous of active galactic nuclei, and are perhaps responsible for quenching star formation in their hosts. The Stripe 82X catalog covers 31.3 deg² of the Stripe 82 field, of which the 15.6 deg² covered with XMM-Newton is also covered by Herschel/SPIRE. We have 2500 X-ray detected sources with multiwavelength counterparts, and 30% of these are unobscured quasars, with $L_{\rm X} > 10^{44}$ erg s $^{-1}$ and $M_{\rm B} < -23$. We define a new population of quasars that are unobscured, have X-ray luminosities in excess of 10^{44} erg s $^{-1}$, have broad emission lines, and yet are also bright in the far-infrared, with a 250 μ m flux density of $S_{250} > 30$ mJy. We refer to these Herschel-detected, unobscured quasars as "cold quasars." A mere 4% (21) of the X-ray- and optically selected unobscured quasars in Stripe 82X are detected at 250 μ m. These cold quasars lie at $z \sim 1$ –3, have $L_{\rm IR} > 10^{12} L_{\odot}$, and have star formation rates (SFRs) of ~ 200 –1400 M_{\odot} yr $^{-1}$. Cold quasars are bluer in the mid-IR than the full quasar population, and 72% of our cold quasars have WISE W3 < 11.5 [Vega], while only 19% of the full quasar sample meets this criteria. Crucially, cold quasars have on average \sim nine times as much star formation as the main sequence of star-forming galaxies at similar redshifts. Although dust-rich, unobscured quasars have occasionally been noted in the literature before, we argue that they should be considered as a separate class of quasars due to their high SFRs. This phase is likely short-lived, as the central engine and immense star formation consume the gas reservoir. Cold quasars are type-1 blue quasars that reside in starburst galaxies.

Unified Astronomy Thesaurus concepts: Far infrared astronomy (529); Quasars (1319); Starburst galaxies (1570)

1. Introduction

The origin of luminous quasars is perhaps a dramatic story, wherein two immense galaxies collide, fueling a burst of star formation and triggering rapid growth of a supermassive black hole (e.g., Hopkins et al. 2006). In the major merger paradigm, the active galactic nucleus (AGN) goes through an obscured growth phase, where the accretion disk is hidden by dust, while the host galaxy experiences a period of enhanced star formation. This phase ends when the AGN launches winds powerful enough to blow away some of the circumnuclear obscuring dust so that the accretion disk becomes visible in the optical as star formation quenches in the host galaxy (Glikman et al. 2004, 2012; Pontzen & Governato 2012). Quasars are the most luminous of AGN, and it has been suggested that they are almost universally produced by major mergers (Treister et al. 2012).

AGN can heat torus and circumnuclear dust to >1000 K, producing IR emission from $\lambda = 1$ –40 μ m (e.g., Elvis et al. 1994; Netzer et al. 2007; Mullaney et al. 2011). Additionally, AGN heat and excite physically extended gas clouds to form the narrow-line region, which in extreme cases of merging galaxies can be larger than the galaxy itself (e.g., Hainline et al. 2016). The narrow-line region contains gas ionized by the

radiation field of the AGN, and it also contains dust (Groves et al. 2006). The emission from the AGN torus or circumnuclear environment typically peaks around 25 μ m, although the exact temperature depends on the incident radiation field and optical depth. In AGN where the central nucleus has a lot of obscuring material, galactic dust can be even colder, peaking at wavelengths longer than 25 μ m, as the incident radiation field is absorbed and reradiated through large column densities. It is possible, in heavily obscured cases, that the AGN can account for all of the far-IR emission (Sajina et al. 2012; Ricci et al. 2017). Such heavily obscured objects are thought to be rare, as the amount of obscuration increases with stellar mass (Buchner et al. 2017; Buchner & Bauer 2017). In the major merger paradigm, heavily obscured phases are likely shortlived (20% of the blue quasar phase), occurring briefly as the quasar is in the transitional blowout phase, after which it becomes optically luminous (Glikman et al. 2012). The guasar lifetime is only weakly constrained through clustering measurements to be $\sim 10^6 - 10^9$ yr (Conroy & White 2013; la Plante & Trac 2016). Further complicating matters, the IR emission in unobscured quasars can vary dramatically from source to source (Lyu & Rieke 2018). Dust can arise from the

torus, narrow-line region (Groves et al. 2006; Mor et al. 2009), or AGN outflows (Murray et al. 2005), and the shape of the IR emission depends sensitively on viewing angle and dust covering fraction. Different models also use smaller ($a=0.005-0.25\,\mu\mathrm{m}$; Fritz et al. 2006) or larger ($a=0.1-1\,\mu\mathrm{m}$; Hönig & Kishimoto 2010) grain sizes and compositions. These assumptions can change the shape of the IR emission, particularly around the silicate absorption lines. However, González-Martín et al. (2019) demonstrate that IR photometry can only distinguish between any models when there is less than 50% contamination from the host galaxy. This is only the case for the nearest sources.

The location of the obscuration in quasars produced by mergers is difficult to tease out, as it can in principal arise from any dust or gas along the line of sight. The traditional torus model places the obscurer in a compact, donut-like structure within a few parsecs of the accretion disk. In the most successful torus models, the torus does not have sharp edges, is physically related to the accretion disk, and is made of clumpy clouds of dust and gas (e.g., Elitzur & Shlosman 2006). Obscured AGN can be the product of a viewing angle through the thicker parts of the torus (Urry & Padovani 1995). The torus is structurally related to the supermassive black hole by being under its gravitational influence, absorbing radiation from the accretion disk, and possibly being formed from winds off of the accretion disk. The host galaxy itself is another source of obscuration. Gas and dust in the host galaxy are not associated with the AGN structure, even if they are circumnuclear. Buchner et al. (2017) and Buchner & Bauer (2017) measured hydrogen column densities from the host galaxy and the AGN and found that the galaxy can account for Compton thin obscuration $(N_{\rm H}=10^{22}\,{\rm cm}^{-2})$ but not Compton thick $(N_{\rm H}>10^{24}\,{\rm cm}^{-2})$. Dust absorption is commonly parameterized by the optical depth of the 9.7 μ m silicate absorption feature (Spoon et al. 2007). High silicate optical depth is observed in obscured AGN, and this dust may arise from the torus (Hatziminaoglou et al. 2015). In local mergers, Goulding et al. (2012) showed that silicate dust absorption correlates with the viewing angle of the host galaxy and not with gas column densities of the AGN measured from the X-ray. Dust and gas obscuration can arise from a foreground screen rather than the AGN structure itself (Hatziminaoglou et al. 2015; Buchner et al. 2017). In fact, mergers in particular exhibit a clear correlation between gas and dust obscuration and merger stage. with late-stage mergers being more obscured (Sanders & Mirabel 1996; Hopkins et al. 2008; Petric et al. 2011; Stierwalt et al. 2013; Ricci et al. 2017).

Quasars may substantially affect the star formation of their host galaxies through feedback processes, though the exact nature of that role remains unclear. In AGN, winds can either blow out the ISM and quench star formation (negative feedback; Hopkins et al. 2006), or they can compress the ISM and trigger star formation (positive feedback; Ciotti & Ostriker 2007). Accretion onto the most massive black holes is observed to produce collimated jets that sweep through the galaxy producing kinetic feedback (Heckman & Best 2014). However, in a limited number of sources, star formation is observed to be enhanced in X-ray-selected and optically selected AGN (Salomé et al. 2015; Mahoro et al. 2017; Perna et al. 2018). Further complicating matters, other studies indicate no link between AGN activity and either enhanced or decreased star formation. For example, Stanley et al. (2017)

find no decrease in star formation rate (SFR) with AGN bolometric luminosity for the optically selected AGN from the Sloan Digital Sky Survey (SDSS). Omont et al. (2003) observes $L_{\rm IR}\sim 10^{13}\,L_{\odot}$, indicating SFRs $>\!1000\,M_{\odot}$ yr $^{-1}$ in quasars at $z\sim 2$. Recently, Schulze et al. (2019) found that 20 unobscured quasars at $z\sim 2$ have no statistically significant difference in SFRs than star-forming galaxies, based on ALMA continuum measurements. In a small local sample, unobscured quasars were shown to have similar dust masses as obscured quasars, indicating that unobscured quasars might not be in a later evolutionary stage (Shangguan & Ho 2019).

One problem in synthesizing literature results into a coherent picture is that selection in different wavelength regimes can produce biased samples (Hickox et al. 2009; Azadi et al. 2017), particularly when studying obscured AGN. As 75% of AGN growth is obscured (Treister et al. 2004; Ananna et al. 2019), these sources provide the most insight into black hole—galaxy coevolution. Unobscured AGN, and in particular quasars, should provide the clearest insight into how massive galaxies die, as unobscured quasars have presumably blown out their own obscuring material. Their immense energies should start to affect their hosts and usher in the passive galaxy phase. But making this connection directly is hard. Precisely because unobscured quasars are so luminous, it becomes very difficult to study their host galaxy properties. Quasars outshine their hosts in the optical and mid-IR photometry (Hainline et al. 2011; Stern et al. 2012). They contaminate the optical emission lines used to study star formation, particularly H_{α} (Baldwin et al. 1981). Submillimeter emission lines, which trace the dense interstellar medium (ISM) in star-forming regions, are also enhanced in AGN (Imanishi et al. 2016; Kamenetzky et al. 2016; Kirkpatrick et al. 2019). The most robust tracer of the host galaxy is therefore the far-IR, as AGN are expected not to be able to heat dust beyond $\lambda > 100 \,\mu\text{m}$, as is evidenced by the sharp drop in far-IR emission seen in X-ray luminous AGN (Mullaney et al. 2011; Rosario et al. 2012). Lyu & Rieke (2017) argue that AGN in fact cannot account for much emission at wavelengths longer than $20 \mu m$, simply due to energy balance arguments.

In this paper, we present an unbiased look at the interstellar medium of unobscured quasars. This is the first in a series of papers examining in detail the multiwavelength emission of X-ray selected AGN with far-IR emission in the Accretion History of AGN survey (AHA 13 ; PI, M. Urry). We discuss the survey and infrared sample selection in Section 2, including our definition of cold quasars. We discuss in Section 3 how the IR emission of cold quasars compares with unobscured quasars. Our conclusions are listed in Section 4. Throughout this paper, we assume a standard cosmology with $H_0=70\,\mathrm{km\,s^{-1}\,Mpc^{-1}},$ $\Omega_\mathrm{M}=0.3,$ and $\Omega_\Lambda=0.7.$

2. A Multiwavelength AGN Survey

Large volumes of the universe must be surveyed in order to discover a representative sample of rare objects like high-luminosity AGN. This paper is part of AHA, which is a multiwavelength survey that assembles data from the Stripe 82X (31 deg²; LaMassa et al. 2013b, 2013a, 2015), COSMOS (2 deg²; Cappelluti et al. 2007; Scoville et al. 2007; Elvis et al. 2009; Civano et al. 2016; Marchesi et al. 2016), and GOODS-South fields (0.1 deg²; Brandt et al. 2001; Giacconi et al. 2002;

¹³ http://project.ifa.hawaii.edu/aha/

Giavalisco et al. 2004). These fields comprise a "wedding cake" tiered X-ray survey, where each cake layer probes a different area and flux limit, and thus a different luminosity-redshift range. Stripe 82X covers the most luminous sources, while COSMOS and GOODS-South contain less luminous and/or more obscured AGN. We focus here on the Stripe 82X component, which has the most luminous X-ray sources in our survey, and will discuss the IR AGN in the full AHA survey in a subsequent paper.

Our team surveyed 4.6 deg² and 15.6 deg² of the SDSS field Stripe 82 with XMM-Newton in AO10 and AO13 (LaMassa et al. 2013a, 2016). We combined these observations with a further 5.6 deg² of XMM-Newton archival pointings and 6.0 deg² of Chandra archival pointings in Stripe 82 for a total Stripe 82X survey area of 31.3 deg². From this catalog, 15.6 deg², covered with XMM-Newton in AO13, is also fully covered by Herschel Space Observatory observations with the SPIRE instrument as part of the Herschel Stripe82 Survey (HerS; Viero et al. 2014). AO13 has coadded exposure times of 6-8 ks (LaMassa et al. 2016). Additionally, there are 125 sources from AO10 that fall in the HerS survey region (LaMassa et al. 2013a). We refer the reader to Figure 1 in Ananna et al. (2017) for the layout of Stripe 82 covered by XMM and Herschel. Multiwavelength counterpart matching was done in LaMassa et al. (2016) and Ananna et al. (2017). The authors use the coadded SDSS catalogs (Jiang et al. 2014; Fliri & Trujillo 2016), which reach 2.5 mag deeper than single epoch data, to increase the likelihood of each X-ray source having an optical counterpart. The authors match the X-ray positions to multiwavelength counterparts spanning the UV to the mid-IR. This portion of Stripe 82 is covered by warm Spitzer (3.6 and 4.5 μ m only) through the Spitzer/HETDEX Exploratory Large Area survey (Papovich et al. 2016), the Spitzer IRAC Equatorial Survey (SpIES; Timlin et al. 2016), and by WISE in the mid-IR. It is also covered in the near-IR by the Vista Hemisphere Survey (McMahon et al. 2013) and the UKIRT Infrared Deep Sky Survey (Lawrence et al. 2007), and in the UV by GALEX. Full details of the observations and counterpart identification can be found in LaMassa et al. (2016) and Ananna et al. (2017). The 16 deg² portion of Stripe 82X that overlaps with the HerS survey area contains 3200 X-ray sources (LaMassa et al. 2016). We remove 295 sources that do not have robust multiwavelength counterparts (and hence photo-zs), as indicated by a counterpart quality flag of three or four in the Ananna et al. (2017) photometric catalog. This leaves 2905 X-ray sources.

2.1. The Herschel/X-Ray Subsample

One of the goals of AHA is to determine the host galaxy properties of the most luminous X-ray sources. This requires unambiguous observations of the host galaxy, which, for unobscured AGN, can best be done at longer wavelengths, such as the far-IR and submillimeter. A luminous AGN can contaminate all other wavelengths. Of the 2905 X-ray sources, 120 galaxies are also detected at 250 μm , which we refer to as the Herschel subsample. The HerS survey has a 3σ detection limit of $S_{250~\mu m}=30~\text{mJy}$ (Viero et al. 2014). In a purely star-forming galaxy, this flux detection limit corresponds to an SFR of $174~M_{\odot}\text{yr}^{-1}$ at z=1 and $758~M_{\odot}\text{yr}^{-1}$ at z=2, estimated using the Kirkpatrick et al. (2012) templates. We summarize the sample selection in Figure 1.

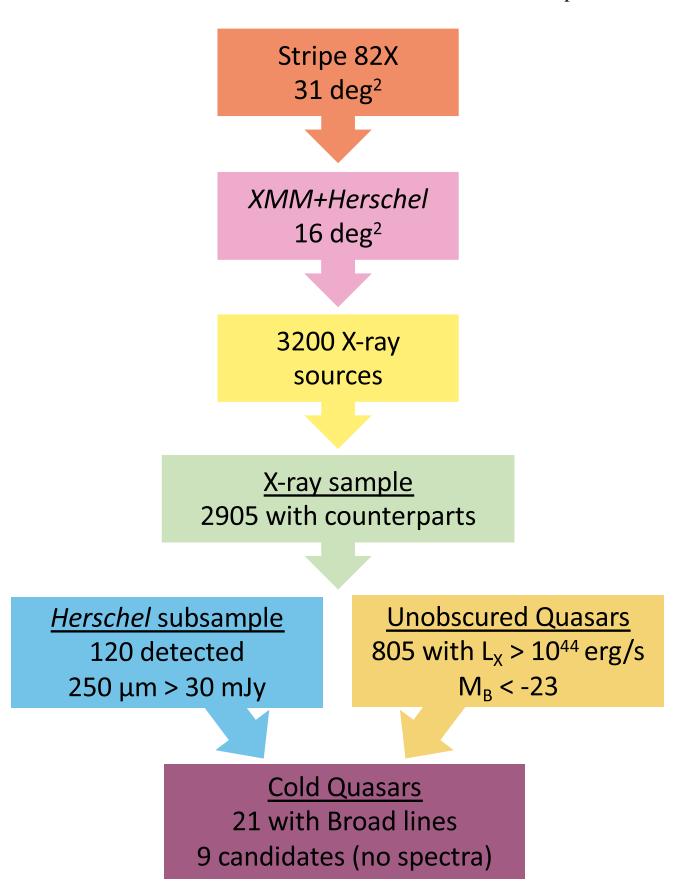


Figure 1. Visual summary of our main sample selection criteria.

Ninety-nine galaxies from the Herschel subsample have spectroscopic redshifts measured from SDSS spectra (from DR12, DR13, or DR14). The remaining 21 have photometric redshifts determined by fitting the UV/optical/NIR data with the LePhare code (Arnouts et al. 1999; Ilbert et al. 2006). We show the full band X-ray luminosity (throughout the text, $L_{\rm X} = L_{0.5-10\,{\rm kev}}$) and redshift distribution of the Stripe 82X sources and Herschel subsample in Figure 2. The X-ray luminosities have been k-corrected using $\Gamma=2.0$ for the hard band and $\Gamma=1.8$ for the soft band (LaMassa et al. 2016), but they are not corrected for absorption.

2.2. Cold Quasar Definition

We find that our Herschel subsample includes many unobscured, luminous AGN. We call unobscured quasars any source with $L_{\rm X} > 1 \times 10^{44}~{\rm erg~s^{-1}}$ and $M_B < -23$ (Schmidt & Green 1983; McDowell et al. 1989). To transform between the SDSS filters and the B band, we used the equation

$$m_B = m_g + 0.17(m_u - m_g) + 0.11$$
 (1)

(Jester et al. 2005). From the full X-ray sample, 805 sources match this definition. We refer to these as the unobscured quasars throughout the text and figures. Of the Herschel subsample, 32 galaxies satisfy these criteria, 23 of which have optical broad lines, confirming that they are type-1 quasars. Two of these sources are blazars, based on their reported radio flux densities in the Very Large Array's FIRST survey (White et al. 1997). These two sources also have 500 μ m emission that is brighter than the 250 μ m emission. This "rising" emission

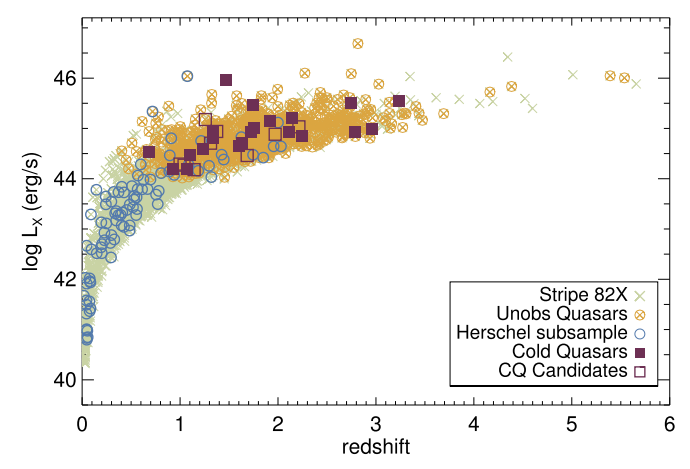


Figure 2. X-ray (0.5–10 kev) luminosity and redshift distribution of the full Stripe 82X sample in the $16 \, {\rm deg^2}$ region of the sky covered by both XMM-Newton and Herschel (light green crosses; 2905 galaxies). The 120 galaxies detected in both the X-ray and at 250 μ m form our Herschel subsample (blue circles). We refer to the X-ray sources with $L_{\rm X} > 1 \times 10^{44} \, {\rm erg \ s^{-1}}$ and $M_B < -23$ as unobscured quasars (orange circles with crosses). The unobscured quasars with a 250 μ m detection make up our cold quasar subsample (purple filled squares). We identify cold quasar candidates as sources that meet the stated definitions but lack optical broad-line emission, either due to not having a spectrum or having a spectrum with a low signal-tonoise ratio.

indicates likely contamination of the far-IR emission from nonthermal sources. We remove these two quasars from the sample. Herein, we create a new definition to categorize quasars. We refer to the remaining 21 galaxies as the "cold quasars." The remaining nine Herschel sources either do not have an SDSS spectrum or have a spectrum with a low signal-to-noise ratio, making it difficult to distinguish broad lines. We refer to these nine galaxies as cold quasar candidates throughout the text. We will analyze all optical spectra from the full Herschel subsample in a future paper (M. Estrada et al. 2020, in preparation).

All cold quasars resemble point sources in the optical and are unresolved in the Herschel bands (Figures 3 and 4). We show all optical and Herschel images on our website (https://kirkpatrick.ku.edu/CQ/). They lie between 0.5 < z < 3.5, due to the extreme X-ray luminosities. We list the properties of the cold quasars in Table 1. All cold quasars are detected in all three Herschel/SPIRE bands.

Red quasars are type-1 quasars that have a red continuum in the optical, indicating a moderate amount of dust (E(B-V)>0.25) along the line of sight that does not fully obscure the broad-line region (Urrutia et al. 2008; Glikman et al. 2013, 2018). These quasars are among the most luminous objects in the universe and are generally found in late-stage mergers (Glikman et al. 2015). Red quasar candidates can be selected using $r_{\rm AB}-K_{\rm Vega}>5$ \wedge J-K>1.5 (Glikman et al. 2013). According to this color selection, none of our

cold quasars or cold quasar candidates are red quasars. We find the cold quasar population is distinct from the red quasar population in that they do not have reddened continua.

2.3. Host Galaxy Properties

We determined the IR luminosities and IR AGN contribution of all Herschel X-ray sources by decomposing the WISE and Herschel photometry into an AGN and host galaxy component. We use the featureless AGN template from Kirkpatrick et al. (2012) and three possible host templates: the $z \sim 1$ starforming template from Kirkpatrick et al. (2012), the submillimeter galaxy template from Pope et al. (2008), and the SB5 template from Mullaney et al. (2011). These three templates were chosen to cover a range in dust temperatures and far-IR to mid-IR emission. The featureless AGN template is derived from the emission of X-ray luminous AGN at $z\sim 1$ –3. Due to the scarcity of data points in the IR, we fit the simplest model possible: model = $N_1 \times \text{AGN} + N_2 \times \text{Host}$, where we allow the normalizations, N_1 and N_2 , to vary simultaneously. We use a χ^2 minimization technique to determine the best fit. Since the photometric uncertainty is large in the mid- and far-IR, we use a Monte Carlo simulation to determine the uncertainties of the model. We randomly sample each data point within its error and refit the model 100 times. The final normalizations are the median of these 100 trials, and the associated uncertainties are the standard deviations. All of the cold quasars are best fit using the submillimeter galaxy template, which has the largest far-IR to mid-IR ratio and is empirically derived from starbursts at z = 1-2. For four cold quasars, we also have to vary the slope of the featureless AGN template to be steeper, indicating more obscuration in the torus. We show all the fits in the Appendix.

The featureless AGN template allows for a large contribution of the far-IR to be from the AGN itself (this template peaks around $\lambda \sim 30~\mu m$). This amount of far-IR heating was determined empirically (Kirkpatrick et al. 2012). Without more data covering the crucial transition range between AGN- and host-dominated emission ($\lambda \sim 10$ –70 μm), it is impossible to further constrain how much of the far-IR originates with the AGN heating. The featureless AGN template accounts for more of the far-IR heating than standard QSO templates (Elvis et al. 1994; Lyu & Rieke 2017). We test how much the $L_{\rm IR}$ and SFR changes when we use the Elvis et al. (1994) Type-1 QSO template, and we find the change to be negligible.

We experimented with more complex fitting methods such as SED3FIT (Berta et al. 2013) and CIGALE (Burgarella et al. 2005; Boquien et al. 2019). The SFRs were generally a factor of 2-3× higher than with our fitting method, and the AGN contribution to the IR was found to be much lower. This is due to the fact that the AGN templates used in both codes fall off around 10 μ m, so they account for a negligible amount of the far-IR heating. For >60% of the sample, we found the UVoptical fitting to be unreliable. Both CIGALE and SED3FIT determined the UV-Optical was dominated by galaxy emission, despite spectral evidence to the contrary. We verified that the optical emission of our cold quasars can be completely accounted for by an unobscured quasar, by scaling the optical luminous QSO template from Richards et al. (2006). All of the cold quasars can be fit with this template, and only four require any extinction, which we model with an SMC-like dust curve (Draine 2003). For these four quasars, E(B-V) < 0.2. When using SED3FIT or CIGALE, the resulting SFRs are high due

¹⁴ We use the DESI Legacy Imaging Surveys (Dey et al. 2019) to create optical images from the *grz* bands of our cold quasars. Our sources lie in the footprint covered by the Dark Energy Camera Legacy Survey (Flaugher et al. 2015), observed by the Dark Energy Camera on the 4 m Blanco telescope at the Cerro Tololo Inter-American Observatory. The Legacy Surveys reach a *z*-band limiting magnitude of 22.5 mag, making them deeper than the images in the SDSS Data Releases. However, we do not use the photometry from the Legacy Surveys for any spectral fitting or analysis.

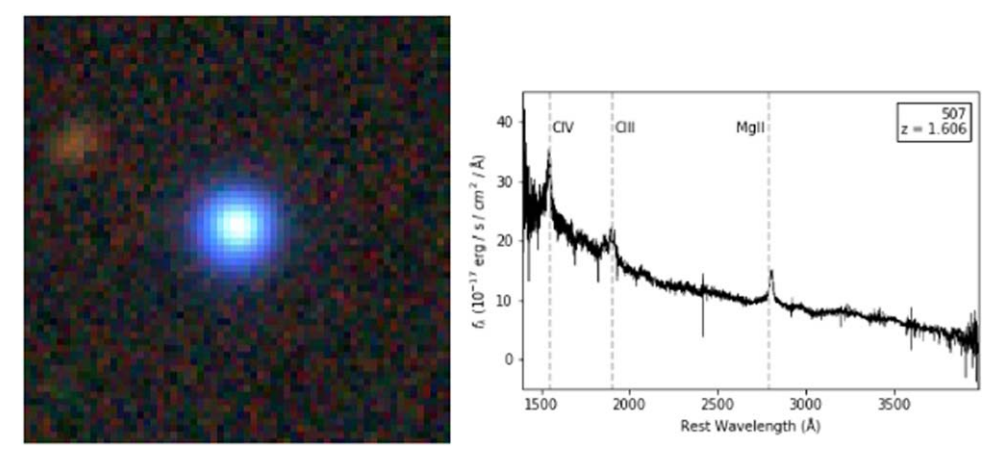


Figure 3. Example of a cold quasar (ID 507, z = 1.606). Left: an RGB image, where blue is the *g*-band filter from the DECam Legacy Survey, green is the *r*-band, and red is the *z*-band. Each side of the image is 20". The blue color indicates that this quasar is not dust reddened. All of our cold quasars are blue point sources. Right: rest frame optical SDSS spectrum with the broad lines labeled. The continuum is blue, and two broad lines are evident. Spectra and images for all Herschel sources are available at https://kirkpatrick.ku.edu/CQ/.

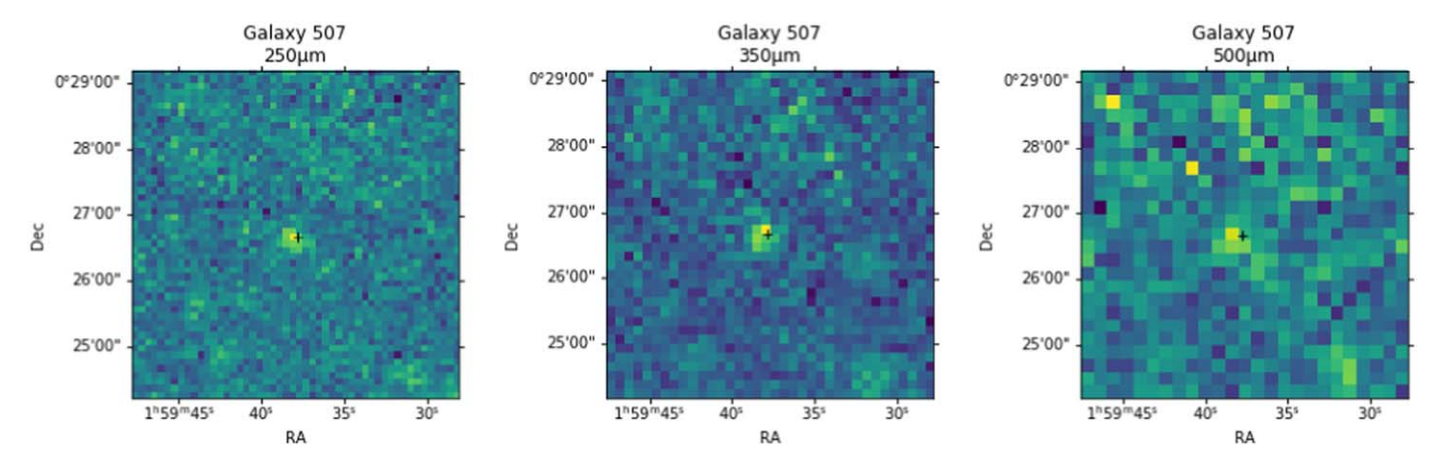


Figure 4. Far-IR emission of cold quasar 507 (z = 1.606). From top to bottom, we show the 250, 350, and 500 μ m Herschel/SPIRE images, with the X-ray position marked with the cross.

to the assumed contribution from unobscured stars in the UV and the slope of the extrapolated longer wavelength emission ($\lambda > 300~\mu m$). Due to these issues, we opted not to use the SED3FIT or CIGALE results. Exploring these discrepancies in more detail will be the subject of a future paper.

We calculate $f_{\rm AGN}$ by integrating under the featureless AGN template to obtain the $L_{\rm IR}$ of the AGN component, and we express this as a fraction of the total $L_{\rm IR}$ (8–1000 μ m). To determine the SFR, we integrate the host galaxy template from 8 to 1000 μ m and then use the relationship from Murphy et al. (2011):

SFR
$$[M_{\odot} \text{ yr}^{-1}] = (1.59 \times 10^{-10}) \times L_{\text{IR}}^{\text{host}} [L_{\odot}].$$
 (2)

In unobscured quasars, the AGN dominates the emission at nearly all wavelengths, making stellar mass notoriously difficult to determine. We estimate M_* from the black hole mass. We obtain M_{\bullet} for 18 of our cold quasars from the SDSS DR7 spectral catalog published in Shen et al. (2011), which includes $L_{\rm bol}$ estimated from the 5100 Å, 3000 Å, and 1350 Å monochromatic luminosity and M_{\bullet} estimated from H β , C IV, or Mg II. We use the relation from Bennert et al. (2011) to

calculate M_* :

$$\log \frac{M_{\bullet}}{10^8 M_{\odot}} = 1.12 \log \frac{M_{*}}{10^{10} M_{\odot}} + (1.15 \pm 0.15) \log(1 + z) - 0.68 + (0.16 \pm 0.06).$$
(3)

We adopt the L_{bol} listed in Shen et al. (2011). For the three galaxies not included in this catalog, we calculated L_{bol} from L_{X} using the following relation from Lusso et al. (2012):

$$\log \frac{L_{\text{Bol}}}{L_{\text{X}}} = -0.020x^3 + 0.114x^2 + 0.310x + 1.296, \quad (4)$$

where $x = \log L_{\rm Bol} - 12$ in solar luminosity units. We list the host galaxy properties IR luminosity ($L_{\rm IR}$ [8–1000 μ m]), stellar mass (M_*), $f_{\rm AGN}$, and SFR in Table 1.

3. Results and Discussion

3.1. Infrared Colors

Mid-IR color-color diagrams are an effective way of identifying luminous AGN (Lacy et al. 2004; Stern et al. 2005;

Table 1Cold Quasar Properties

ID ^a	R.A. (J2000)	Decl. (J2000)	Z	$\frac{\log L_{0.5-10~\mathrm{keV}}}{(\mathrm{erg~s}^{-1})}$	$\log L_{\rm bol} \atop ({\rm erg~s}^{-1})$	$\log L_{ m IR} \ (L_{\odot})$	f _{AGN} (8–1000 μm)	$\log M_* \ (M_{\odot})$	$SFR (M_{\odot} \text{ yr}^{-1})$
475	01:19:48.4	+00:43:54.28	1.754	45.01	46.85 ± 0.01	13.41 ± 0.05	0.86 ± 0.13	12.00 ± 0.12	588 ± 112
507	01:59:37.8	+00:26:39.91	1.606	44.64	46.60 ± 0.01	13.07 ± 0.03	0.56 ± 0.04	10.80 ± 0.13	835 ± 102
2435	00:57:43.7	-00:11:57.92	1.067	44.19	45.78 ± 0.01	12.69 ± 0.03	0.21 ± 0.02	10.21 ± 0.78	616 ± 56
2480	00:58:28.9	+00:13:45.25	1.239	44.59	45.87 ± 0.01	12.53 ± 0.07	0.55 ± 0.09	10.69 ± 0.11	240 ± 79
2551	00:59:46.6	+00:02:54.61	0.682	44.54	45.63 ± 0.03	12.41 ± 0.04	0.45 ± 0.04	10.89 ± 0.10	226 ± 36
2651	01:01:13.3	-00:29:45.20	1.337	44.80	46.11 ± 0.01	12.60 ± 0.06	0.52 ± 0.08	10.98 ± 0.16	306 ± 82
3122	01:09:01.0	+00:01:37.44	2.955	44.98	46.78 ± 0.20^{b}	13.51 ± 0.04	0.73 ± 0.07		1393 ± 299
3716	01:19:00.4	-00:01:57.68	2.750	45.50	47.85 ± 0.20^{b}	13.48 ± 0.03	0.79 ± 0.05		976 ± 243
3819	01:21:10.0	-00:29:10.36	1.719	44.92	46.25 ± 0.01	12.67 ± 0.07	0.43 ± 0.07	10.90 ± 0.15	428 ± 117
3871	01:22:49.7	-00:07:07.13	1.631	44.71	46.14 ± 0.01	12.64 ± 0.16	0.48 ± 0.18	11.27 ± 0.16	358 ± 251
4077	01:30:34.0	-00:21:06.61	3.234	45.55	47.95 ± 0.20^{b}	13.15 ± 0.10	0.36 ± 0.09		1435 ± 511
4252	01:35:54.4	-00:22:31.91	2.249	44.85	46.46 ± 0.03	13.01 ± 0.06	0.34 ± 0.05	10.71 ± 0.62	1062 ± 197
4285	01:37:26.4	+00:11:52.45	1.103	44.47	46.20 ± 0.00	12.64 ± 0.05	0.60 ± 0.07	10.84 ± 0.14	276 ± 73
4324	01:38:14.7	+00:00:05.78	2.144	45.20	46.92 ± 0.01	13.35 ± 0.07	0.65 ± 0.18	11.43 ± 0.13	1255 ± 153
4336	01:38:25.3	-00:05:34.39	1.341	44.94	46.73 ± 0.00	12.95 ± 0.03	0.78 ± 0.05	11.17 ± 0.10	315 ± 79
4472	01:40:33.8	+00:02:30.05	1.921	45.15	46.19 ± 0.04	13.06 ± 0.04	0.46 ± 0.04	10.45 ± 0.19	995 ± 150
4668	01:43:01.9	-00:26:56.54	2.786	44.93	47.01 ± 0.01	13.32 ± 0.06	0.68 ± 0.09	11.20 ± 0.12	1070 ± 416
4979	01:08:21.1	-00:02:28.51	0.930	44.19	46.20 ± 0.00	12.44 ± 0.06	0.63 ± 0.09	10.52 ± 0.14	162 ± 59
5074	01:49:40.2	+00:17:17.76	1.464	45.95	46.73 ± 0.00	12.88 ± 0.03	0.74 ± 0.06	11.05 ± 0.12	309 ± 87
5097	01:49:58.3	-00:30:25.00	2.111	44.94	46.37 ± 0.03	13.22 ± 0.08	0.64 ± 0.21	10.98 ± 0.16	949 ± 145
5122	01:50:34.5	-00:02:00.46	1.740	45.47	46.54 ± 0.01	13.29 ± 0.05	0.76 ± 0.13	10.31 ± 0.86	725 ± 124

Notes.

Donley et al. 2012; Mateos et al. 2012; Stern et al. 2012). The AGN typically has a torus that produces redder mid-IR colors than purely star-forming galaxies (Donley et al. 2012). Twenty cold quasars are detected in the W1 and W2 bands, and all of these meet the WISE AGN selection criteria W1-W2>0.5 from Assef et al. (2018), which was designed to select AGN with a completeness of 90% (dashed line; Figure 5). They also satisfy the criteria

$$W1 - W2 > 0.53 \exp[0.183(W2 - 13.76)^2]$$
 (5)

from Assef et al. (2018), which was designed to select AGN with a reliability of 90% (dotted–dashed line; Figure 5). In other words, our cold quasars have the near- and mid-IR emission expected of luminous AGN. A subset of mid-IR AGN are defined as hot dust-obscured galaxies (Hot DOGS; Eisenhardt et al. 2012). These are rare, dusty galaxies with $L_{\rm IR} > 10^{13} \, L_{\odot}$ (Wu et al. 2012). Hot DOGs are luminous quasars, yet dust obscured. Hot DOGs are also referred to as W1W2 dropouts due to their extremely red spectrum and are typically selected according to W1 > 17.4 and W2 - W4 > 8.2 (Eisenhardt et al. 2012). None of our cold quasars meet the WISE selection criteria to be classified as Hot DOGs.

Of the parent unobscured quasar sample, 559 galaxies have W1 and W2 detections. Almost all meet the Assef et al. (2018) completeness criterion shown in Figure 5, but only 57% satisfy the reliability criterion. Our cold quasars lie to the upper left in the distribution of unobscured quasars in Figure 5. This means that they are in general both brighter in the near-IR (W1 and W2 trace near-IR emission at the redshifts of our sources) and redder than the average unobscured quasar in our survey. The median (standard deviation) W1 - W2 color of the cold

quasars is 1.22 (0.17), while the median (standard deviation) of the unobscured quasars is 1.11 (0.27).

The cold quasars are also more luminous in the longer wavelength WISE bands than the unobscured quasars (Figure 6). At $z\sim 1$ –2, where the majority of our cold quasars lie, W3 spans $\lambda\sim 4$ –6 μ m, where the torus should outshine stellar emission. Through examining our sources, we find that 13 cold quasars (out of 18 detected in WISE) satisfy the criterion W3<11.5 [Vega]. We determined this threshold by calculating the expected W3 emission of infrared-selected AGN at z=3.2, the redshift of the most distant cold quasar. We scale the featureless AGN template from Kirkpatrick et al. (2012), which is empirically derived from IR AGN at z=1–3, to $S_{250~\mu m}=30$ mJy, the detection limit of the HerS survey, and calculate the observed W3 magnitude to be 11.5.

In contrast, only 19% of the unobscured quasars have W3 < 11.5. Combining the X-ray and optical quasar criteria with the mid-IR criterion weeds out star-forming galaxies, which can be bright in W3 at $z \sim 0$ –1 due to the 6.2, 7.7, and 11.2 μ m PAH features falling in this bandpass. In fact, many galaxies in our Herschel subsample show significantly enhanced W3 emission, but their low $L_{\rm X}$ ($<10^{42}\,{\rm erg~s^{-1}}$) and IR SED fitting indicate that they are star-forming galaxies. Due to the selection efficiency, the criteria

$$L_{\rm X} > 10^{44} \,{\rm erg \ s^{-1}}$$
 (6)

$$M_B < -23 \tag{7}$$

$$W3 < 11.5$$
 (8)

can be used to select cold quasar candidates for longer wavelength follow-up in future surveys.

^a The ID is the Rec_No from LaMassa et al. (2016).

^b The bolometric luminosity is determined by Equation (4).

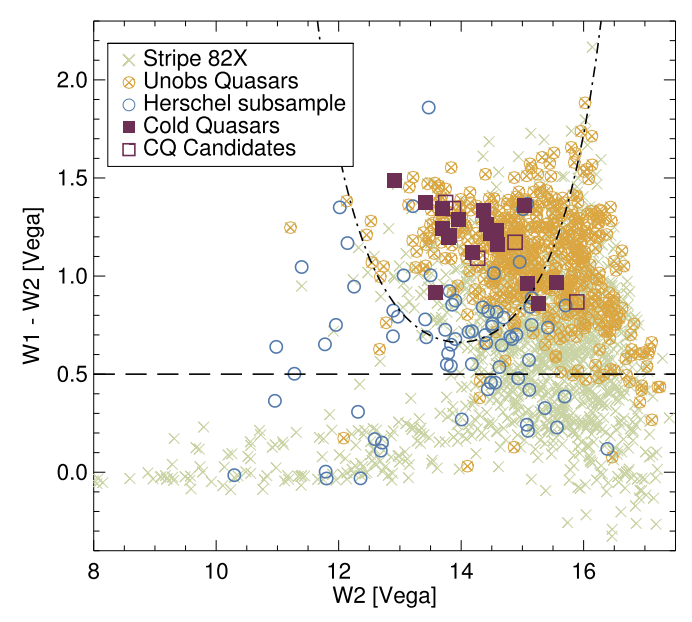


Figure 5. Our Stripe 82X sample in WISE colorspace. Our Herschel subsample (blue circles) is a mix of galaxies dominated by AGN in the mid-IR as opposed to star formation. This is expected given the range of X-ray luminosities in this sample. All the cold quasars (solid purple squares) and cold quasar candidates (unfilled purple squares) lie above the dashed line, which is defined as having a 90% AGN selection completeness in Assef et al. (2018). Most meet the more stringent 90% reliability selection (dotted–dashed line) as well. From our parent Stripe 82X sample (green crosses), we plot unobscured quasars $(L_{\rm X}>10^{44}\,{\rm erg\,s^{-1}},\,M_B<-23)$ as the orange circles with crosses. The cold quasars are generally brighter and redder than the unobscured quasars.

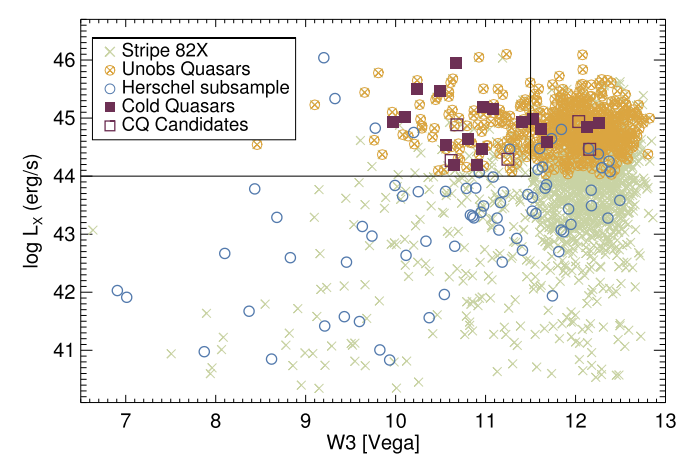


Figure 6. Cold quasars (purple squares) are brighter in the longer wavelength WISE bands than typical unobscured quasars (orange circles with crosses). The full Herschel subsample (blue circles) has a range of W3 magnitudes, but many of the lower $L_{\rm X}$ sources are star-forming galaxies, which have enhanced W3 due to PAH emission. We recommend using $L_{\rm X} > 1 \times 10^{44}$ erg s⁻¹ and W3 < 11.5 (solid lines) to select cold quasar candidates.

The shape of the mid-IR SED is directly related to physical properties of the torus. In a two-component model, where the torus is composed of a smooth disk surrounded by clumps of dust, the slope of the mid-IR emission depends strongly on the optical depth of both the disk and the clumps (Siebenmorgen et al. 2015). We show the slope of the mid-IR SED, parameterized by the color W2-W4 as a function of redshift in Figure 7. At $z\sim 1$ –2, W4 is tracing $\lambda\sim 7$ –11 μm and W2 is tracing $\lambda\sim 1.5$ –2.5 μm . Cold quasars have a bluer W2-W4

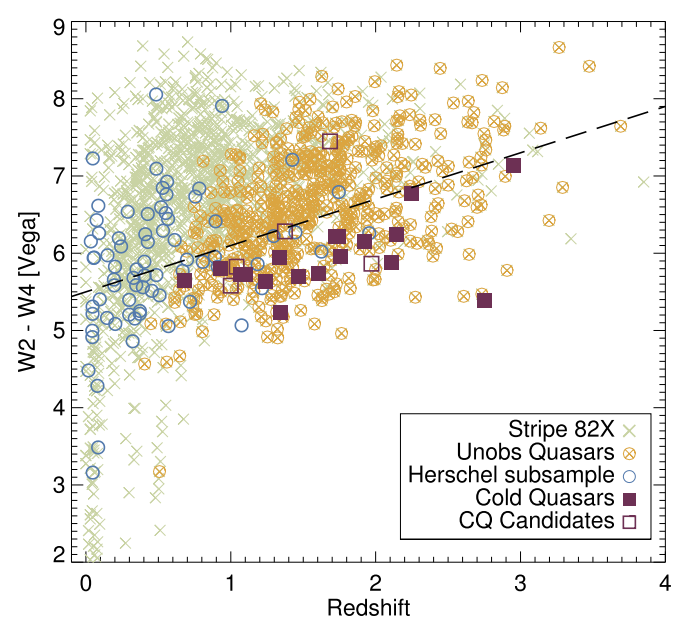


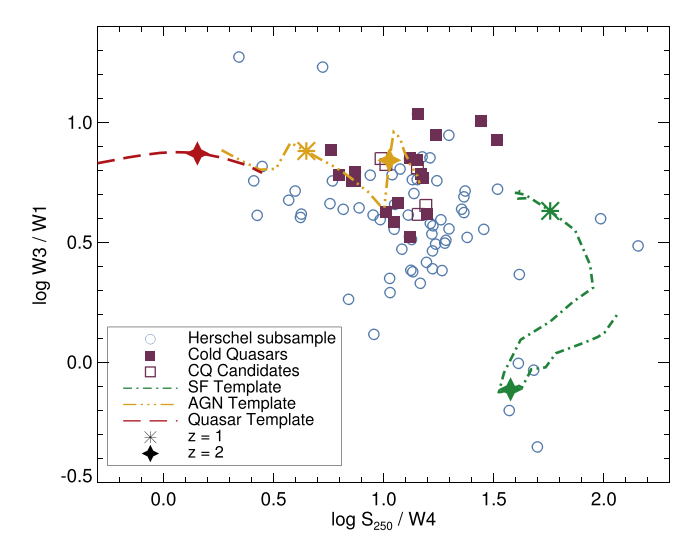
Figure 7. We show the slope of the mid-IR emission, parameterized as W2 - W4, as a function of redshift. Our cold quasars (purple squares) have bluer colors than the unobscured quasars in the parent sample (orange circles with crosses). All cold quasars lie below W2 - W4 = 0.6z + 5.5, plotted as the dashed line. The bluer colors may be due to a torus with a small optical depth, patchy circumnuclear dust, or increasing contribution to the mid-IR colors from star-forming regions.

color than the majority of unobscured quasars at similar redshifts. In fact, all cold quasars lie below the relation

$$W2 - W4 = 0.6z + 5.5 \tag{9}$$

plotted as the dashed line. Only 40% of the unobscured quasars lie below the line. This may indicate that cold quasars have different torus properties, specifically with a lower optical depth, than typical unobscured quasars, or a more face-on viewing angle. Alternately, if the primary obscuring material in blue quasars is circumnuclear, rather than a torus, this indicates a low covering fraction of circumnuclear dust. Of course, sources with a lot of star formation will have bluer W2 - W4colors at $z \sim 1-2$, as W4 will be tracing the continuum in between the 11.2 and 7.7 μ m PAH peaks, while W2 is tracing the stellar emission, which is a maximum around $1.6 \mu m$ (Kirkpatrick et al. 2012). Cold guasars have high SFRs and may be expected to have a significant contribution to their mid-IR emission from star formation, although this is not indicated by the SED fits. More coverage of the mid-IR (e.g., with the James Webb Space Telescope) can tightly constrain how much is due to PAH emission.

Mid-IR bright AGN in star-forming host galaxies will have significant far-IR emission attributable to the host. Kirkpatrick et al. (2013) examined the IR colors of dusty star-forming galaxies, some of which host AGN, from $z \sim 1$ –3. AGN are easily distinguished from star-forming galaxies using dust temperature, measured from the ratio of mid- to far-IR data. AGN-heated dust is much warmer than cool interstellar dust where stars form. With Spitzer and Herschel, the colors $S_{250\mu m}/S_{24\mu m}$ versus $S_{8\mu m}/S_{3.6\mu m}$ reliably separate type-1 and type-2 AGN from star-forming galaxies by tracing the heating sources of the ISM and looking for hot dust from the torus,



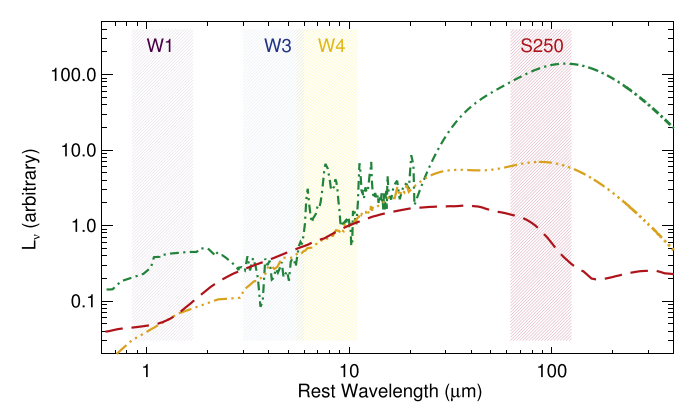


Figure 8. Top panel: $S_{250}/W4$ traces the cold to warm dust, or average dust temperature, while W3/W1 traces the slope of the continuum emission. We plot redshift tracks from z=0.5–3 of a star-forming template (green dotted–dashed line), AGN template (orange dotted–dashed–dotted line; Kirkpatrick et al. 2012), and unobscured quasar template (red dashed line Elvis et al. 1994) to illustrate how star-forming galaxies separate from AGN in this color diagram. Cold quasars (purple filled squares) have similar dust continua but warmer dust than typical unobscured quasars, as do other Herschel-detected sources (blue circles). Bottom panel: we visually compare the three templates plotted in the top panel, normalized at $10~\mu m$. We illustrate with the shaded regions which portion of the SED is covered by the W1, W3, W4, and S_{250} filters at z=1–3.

which produces a steeper continuum in AGN (Kirkpatrick et al. 2013, 2015).

In place of Spitzer/MIPS and IRAC observations, we use $S_{250}/W4$ to trace the ratio of cold dust to warm dust, and W3/W1 to trace the slope of the mid-IR continuum, and we have converted all WISE Vega magnitudes to fluxes. In the top panel of Figure 8, we show where the cold quasars and Herschel subsample lie in this colorspace. We plot the redshift tracks from z=0.5–3.0 of the $z\sim1$ star-forming template and featureless AGN template from Kirkpatrick et al. (2012). These templates were empirically created from 151 star-forming galaxies and AGN with Spitzer and Herschel observations at $z\sim1$ –3. A few sources in our Herschel subsample lie in the region occupied by the star-forming template, and unsurprisingly, these are the sources with $L_{\rm X}<10^{42}$ erg s⁻¹. The cold quasars all occupy the same region as the AGN template, while much of the Herschel subsample lies between the two regimes, indicated a mix of star formation and AGN emission in the mid-IR. The AGN template was derived from sources from the

Chandra Deep Field South at $z \sim 1$ –2. These sources were identified as AGN on the basis of strong power-law emission in their Spitzer/IRS spectra. 75% have $L_{\rm IR} > 10^{12}\,L_{\odot}$. Of these 75%, only 50% have $L_{\rm X} > 10^{44}$ erg s⁻¹ (Brightman et al. 2014), and none meet the optical quasar definition, based on ACS photometry from the Hubble Space Telescope (Giavalisco et al. 2004). They are therefore a fundamentally different population than our cold quasars, and yet have similar ratios of far-IR emission.

We also plot a standard type-1 quasar template from Elvis et al. (1994). This template was created using the IRAS emission of UV and X-ray selected quasars, many of which are part of the Palomar-Green Survey (Green et al. 1986). Lyu & Rieke (2017) compare multiple type-1 quasar templates from the literature and determine that the templates of Elvis et al. (1994), Symeonidis et al. (2016), and Netzer et al. (2007), which are all based on the Palomar-Green Survey, accurately represent the emission of unobscured quasars, while the Kirkpatrick et al. (2012) templates are not valid for luminous type-1 objects. The Palomar-Green Survey is comprised mainly of low redshift quasars (z < 0.2), which show a decline in far-IR emission beyond $\lambda > 20 \,\mu\text{m}$. However, the Elvis et al. (1994) template falls to the left of our sample, indicating that on average, low redshift unobscured quasars have much less cold dust than our cold quasars, which are all at z > 0.5. In the bottom panel of Figure 8, we compare the Elvis et al. (1994) template with the AGN and star-forming template from Kirkpatrick et al. (2012). We illustrate with the shaded regions which portion of the SED is covered by the W1, W3, W4, and S_{250} filters at z = 1-3.

Our cold quasars demonstrate that luminous, type-1 AGN can have an abundance of cold dust, albeit only rarely. The amount of cold dust may partially be attributed to the rising gas fractions of galaxies with redshift, so that local quasar templates cannot be compared to higher redshift quasars (e.g., Geach et al. 2011; Kirkpatrick et al. 2017).

3.2. Are Cold Quasars Special?

We have defined cold quasars as unobscured type-1 quasars with a substantial amount of cold dust ($S_{250} > 30 \,\mathrm{mJy}$). Such galaxies have been observed before in the literature (Frayer et al. 1998; Barvainis & Ivison 2002; Omont et al. 2003; Page et al. 2004; Willott et al. 2007; Coppin et al. 2008; Stacey et al. 2010; Ivison et al. 2019; Simpson et al. 2019) so herein we discuss whether dusty, unobscured quasars deserve their own unique classification. Our cold quasars all have intense SFRs, with the most extreme being $\sim 400 \, M_{\odot} \, \mathrm{yr}^{-1}$. But does it make sense to identify these quasars as a separate class? Answering this question requires that we understand the expected amount of infrared emission in unobscured quasars, which is in itself a difficult question. There are 805 Stripe 82X sources with $L_{\rm X} > 10^{44}\,{\rm erg~s^{-1}}$ and $M_B < -23$. Cold quasars are 3% of this population. If we include the candidates, this rises to 4%. Based on detectability in the far-IR, cold quasars are indeed a special, rare population. Of course, these numbers depend sensitively on the depth of the Herschel data in Stripe 82, and a deeper survey may uncover more cold quasars.

The relatively low sensitivity of Herschel means that only the most luminous infrared galaxies are detected with increasing redshift, even in the deepest fields (e.g., Elbaz et al. 2011). One way around Herschel detection limits is through stacking. Stanley et al. (2017) compile composite IR

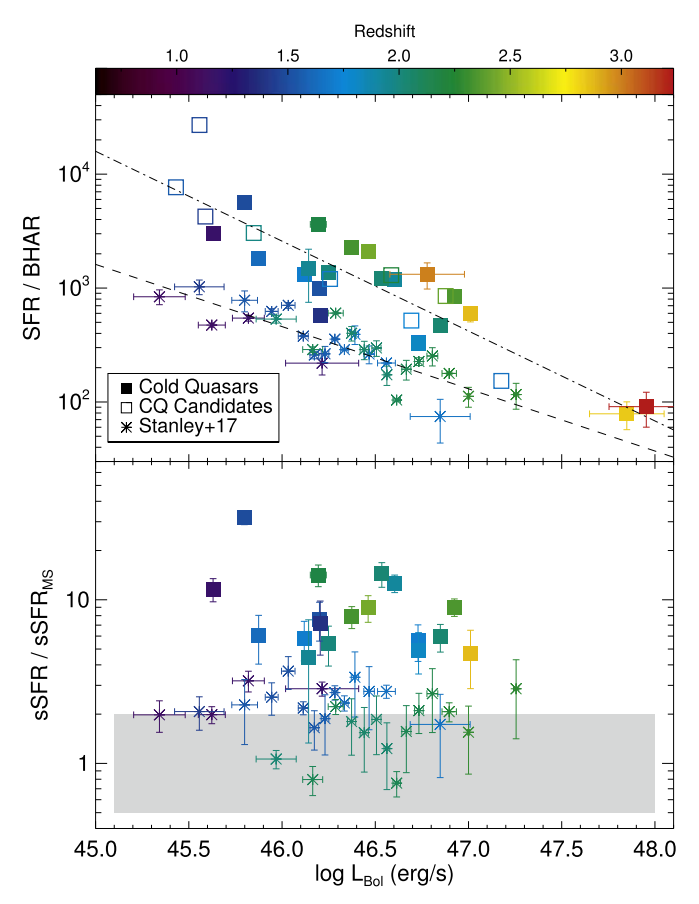


Figure 9. Top panel: $L_{\rm Bol}$ vs. SFR/BHAR for the cold quasars (filled squares), cold quasar candidates (unfilled squares), and stacked unobscured quasars from Stanley et al. (2017). Colors correspond to redshift. The stars are the averages of ~90 quasars each. On average, the cold quasars have 50% as much star formation as the unobscured quasars at the same bolometric luminosities. The dashed line shows the fit to the stars, while the dotted–dashed line is the fit to the cold quasars and cold quasar candidates. Bottom panel: $L_{\rm Bol}$ vs. SFR/SFR_{MS}, where SFR_{MS} is the SFR a galaxy on the main sequence would have, accounting for both M_* and z. The shaded region shows a factor of two above and below the main sequence. There is no trend with $L_{\rm Bol}$. The cold quasars on average lie nine times above the main sequence, while the Stanley et al. (2017) unobscured quasars lie ~two times above the main sequence.

SEDs by stacking Herschel images and averaging WISE fluxes for 3000 optical SDSS unobscured AGN. They measure the average AGN bolometric luminosity, $L_{\rm Bol}$, using the optical spectroscopic values from the SDSS DR7 catalog in Shen et al. (2011) and the stellar mass using M_{\bullet} from Shen et al. (2011) and Equation (4). Stanley et al. (2017) determine the SFR by decomposing the stacked WISE and Herschel photometry using the DecompIR code from Mullaney et al. (2011). As discussed in Kirkpatrick et al. (2012) and Kirkpatrick et al. (2015), the featureless AGN template we use to decompose the cold quasars is remarkably similar to the Mullaney et al. (2011) AGN model.

The Stanley et al. (2017) sample is unbiased with respect to IR detections, and so we presume that their SFRs represent the typical SFR of unobscured quasars of a given bolometric luminosity. We compare our cold quasars and Herschel subsample with the Stanley et al. (2017) sample in Figure 9. We find that our cold quasars have a 50% higher SFR for a given $L_{\rm Bol}$. To make this more obvious, we plot the ratio of SFR to black hole accretion rate (BHAR) as a function of $L_{\rm Bol}$.

We calculate BHAR as

$$BHAR = \frac{(1 - \eta)L_{bol}}{\eta c^2},$$
(10)

where $\eta=0.1$ is the radiative efficiency (Soltan 1982). It is important to bear in mind that the stars in Figure 9 are averages of ~ 90 quasars each, where the error bars represent the standard deviation. Our cold quasars lie above these averages and standard deviations.

Galaxy SFR and evolution are commonly understood in the context of the main sequence, which is the tight relationship between SFR and M_* exhibited by most galaxies (Elbaz et al. 2007; Noeske et al. 2007). In the major merger paradigm, mergers trigger starbursts, significantly elevating SFR above the main sequence (Sanders & Mirabel 1996). The quasar phase is predicted to follow the starburst phase (Hopkins et al. 2007). For typical unobscured quasars, Stanley et al. (2017) find no significant difference between their SFRs and those of star-forming galaxies on the main sequence at similar redshifts. We calculate the distance of the cold quasars and the Stanley et al. (2017) stacks from the main sequence. The main sequence evolves with redshift, and it flattens at higher M_* . We use the relationship between M_* and SFR parameterized in Lee et al. (2015) at z = 1.2:

logSFR_{MS} = 1.72 - log
$$\left[1 + \left(\frac{M_*}{2 \times 10^{10} M_{\odot}} \right)^{-1.07} \right]$$
 (11)

and then we renormalize depending on redshift (Speagle et al. 2014):

$$SFR_{MS}(z) = \left(\frac{1+z}{1+1.2}\right)^{2.9} \times SFR_{MS}(z=1.2).$$
 (12)

We plot SFR/SFR_{MS} as a function of L_{Bol} in the bottom panel of Figure 9. The shaded region illustrates a factor of 2 above and below the main sequence. Dusty star-forming galaxies with $L_{\rm IR}=10^{11}$ – $10^{12}\,L_{\odot}$ typically lie on the main sequence (Casey et al. 2014). On average, our cold quasars have $SFR/SFR_{MS} = 9.3$, with a standard deviation of 6.4. The Stanley et al. (2017) sample has a weighted mean of $SFR/SFR_{MS} = 2.1$, where the points are weighted by the number of galaxies comprising each one. The cold quasars are nine times above the main sequence, well into the starburst regime (e.g., Elbaz et al. 2011). Cold quasars can be understood to be unobscured, type-1 quasars that lie in the starbursting regime of the main sequence. Again, we remind the reader that our SFRs are likely lower limits, since the choice of AGN template includes a significant amount of far-IR heating. Additional observations with far-IR telescopes (e.g., NASA/SOFIA) can help constrain this. Our cold quasars have nearly five times as much star formation than the average unobscured quasar at the same bolometric luminosity.

Finally, we consider whether cold quasars show the expected amount of mid-IR emission given their X-ray luminosity in Figure 10. We calculated $\nu L_{6\mu m}$ by interpolating between the WISE fluxes. We note that the AGN dominates the emission at these wavelengths (see fits in the Appendix), so there is no need to remove the host contribution before interpolating. The relationship between mid-IR luminosity (parameterized by $\nu L_{6\mu m}$) and hard (2–10 kev) X-ray luminosity has been

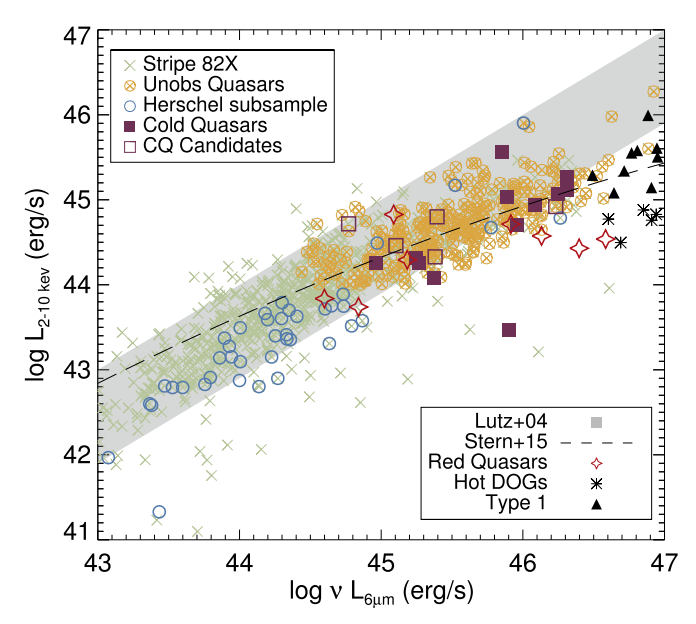


Figure 10. Hard X-ray luminosity as a function of 6 μ m luminosity. We plot the relationship derived from local galaxies (gray shaded region), the relationship derived from higher luminosity, higher redshift sources (dashed line), and several different populations compiled in Glikman et al. (2018). The cold quasars predominantly follow the expected relations and have more X-ray emission relative to the red quasars and Hot DOGs. This indicates less gas absorption in the cold quasars.

quantified for local sources (Lutz et al. 2004) and highluminosity sources (Stern 2015). Sources that lie below the expected relationship (shaded region and dashed line) are underluminous in the X-ray. They can be either Compton thick or perhaps accreting above the Eddington limit, which may be the case for Hot DOGs (Ricci et al. 2017; Wu et al. 2018). However, except for one source, our cold quasars lie around the expected relations derived in both Lutz et al. (2004) and Stern (2015). The outlier is source 507, which has a soft X-ray luminosity (0.5-2 keV) four times greater than the hard X-ray luminosity, but with a blue optical spectrum. It is possible that the hard X-ray luminosity has been underestimated in this source. The cold quasars have enhanced X-ray emission compared to the red quasars (green stars) and Hot DOGs (black asterisks) from LaMassa et al. (2017) and Glikman et al. (2017, 2018), particularly at $\nu L_6 > 10^{46} \ {\rm erg \ s^{-1}}$. However, they follow the same trend as type-1 quasars (black triangles; Glikman et al. 2018). νL_6 traces the amount of hot dust from the torus, while L_X is sensitive to gas absorption. For a given νL_6 , cold quasars have less gas absorption than red quasars. Similar to the red quasars, local merging ultra-luminous galaxies are also underluminous in the X-rays compared with the infrared, indicating a high degree of absorption attributable to the merger (Teng et al. 2015).

In the major merger framework, obscured quasars are understood to be a specific phase of a massive galaxy's life right before blowout (Hopkins et al. 2007; Glikman et al. 2015; Kocevski et al. 2015). Tidal tails and train wreck merger signatures are still visible in red quasars, which have gas absorption visible through lower X-ray emission and redder optical continua (Glikman et al. 2015). High gas column densities are also observed in local major mergers of massive dusty galaxies, many of which harbor obscured AGN (Petric et al. 2011; Teng et al. 2015). On the other hand, Dai et al. (2014) identify a large population of blue broad-line quasars at

 $z\sim 1{\text -}3$ detected at 24 μm , which have clear merger signatures, illustrating that mergers do not universally obscure the central AGN. Within the merging paradigm, the rare cold quasars we have defined are perhaps in a critical transition phase where the AGN growth coexists peacefully within a starbursting galaxy for a brief epoch before quenching. Cold quasars may immediately follow the red quasar stage, where a quasar wind has swept through the inner galaxy, removing the dust, but has not yet reached the star-forming outskirts.

Crucial to understanding the evolutionary stage of cold quasars is understanding where the dust lies and the morphology of the host galaxy. ALMA observations of submillimeter galaxies at $z \sim 2-3$ have revealed that the dust is compact, more so than the gas, mainly lying within 1-3 kpc of the galaxy center (Hodge et al. 2016; Rujopakarn et al. 2016; Hodge et al. 2019; Rujopakarn et al. 2019). If the same is true for cold quasars, then perhaps the quasar has managed to punch a hole in the dust, producing a blue color. In that case, cold quasars may simply be patchy red quasars, rather than a separate evolutionary phase altogether. Red quasars have clear merger signatures, so one way to test this hypothesis is to obtain sensitive observations of the ISM, where the quasar will not outshine the host galaxy, and look for disturbed morphological features. On the other hand, the quasar source may not be cospatial with the far-IR source responsible for the Herschel/SPIRE emission. If cold quasars are in the middle of a merger, the quasar portion could be significantly offset from the wet portion of the merger responsible for the burst of star formation (Fu et al. 2017). Currently, the spatial extent of submillimeter emission from quasars is unknown. ALMA observations of the spatial distribution of the ISM in these galaxies is required to both look for fueling signatures, such as tidal tails, and determine the location of the dust and gas.

If indeed red quasars, cold quasars, and blue quasars are linked together in an evolutionary sequence, the life cycle may be 3%–4% of the blue quasar phase, which is loosely constrained to be 10^6 – 10^9 yr (Conroy & White 2013; la Plante & Trac 2016). For comparison, the red quasar phase is 20% of the blue quasar phase (Glikman et al. 2012). We have based our estimation on considering only those unobscured quasars that lie in the same redshift range as our cold quasars. Tighter constraints can be placed with a mass-matched sample, but we currently lack stellar mass estimates for the full Stripe 82X catalog. If the blue quasar phase lasts a gigayear, then cold quasars may last only $40\,\mathrm{Myr}$.

4. Conclusions

We present a rare sample of X-ray and optically selected broad-line quasars that are detected in all three Herschel/SPIRE bands. We define cold quasars to be broad-line AGN with $L_{\rm X} > 10^{44}\,{\rm erg~s}^{-1},\,M_B < -23,$ and $S_{250} > 30\,{\rm mJy}.$ Our findings are:

- 1. Cold quasars and cold quasar candidates comprise 4% of the unobscured quasar population in Stripe 82X. If understood through the merger-driven paradigm, the duration may be 4% of the blue quasar phase.
- 2. Cold quasars have enhanced mid-IR emission relative to most unobscured quasars. *W*3 < 11.5 [Vega] is an efficient mid-IR selection criteria for cold quasar candidates, selecting 72% of our cold quasars but only 19% of the full unobscured quasar population. This

implies they have considerably more dust and possibly less circumnuclear obscuration than typical unobscured quasars.

- 3. Cold quasars also have a bluer mid-IR spectra than the average unobscured quasar, and the color W4-W2 can also be used to select cold quasar candidates. This blue color may be due to a torus with a lower optical depth than is typical of unobscured quasars, or it may be due to contamination of the mid-IR by the strong star formation emission in these galaxies.
- 4. Cold quasars have significantly more cold dust, as traced by $S_{250~\mu m}$, than expected based on lower redshift unobscured quasars. The amount of cold dust is consistent with that measured in mid-IR selected AGN at $z \sim 1$ –2. The cold dust can be attributed to star formation, and cold quasars have high SFRs of ~ 100 –400 M_{\odot} yr⁻¹.
- 5. The substantial SFRs of cold quasars are nearly five times higher than the average unobscured quasar at the same redshift. Cold quasars lie well off the main sequence (on average, their SFRs are nine times higher than the main sequence) and qualify as starburst galaxies. Whether these immense AGN luminosities and SFRs are triggered by major mergers will require high-resolution submillimeter follow-up with ALMA.
- 6. Cold quasars are best defined as blue type-1 quasars that exist in starbursting galaxies.

This exciting population of unobscured quasars with significant amounts of cold dust could represent a transition phase between dust-obscured quasars and unobscured quasars

that have already depleted their interstellar medium. Further observations of the ISM will provide a more complete picture of how close these sources are to quenching.

We thank the anonymous referee for helpful direction in improving this work. A.K. thanks Rob Ivison and Ian Smail for their generous insights and conversations, which have added detail to this paper. This research is based upon work supported by NASA under award No. 80NSSC18K0418 to Yale University and by the National Science Foundation under grant No. AST-1715512. E.T. acknowledges support from FONDECYT Regular 1160999 and 1190818, CONICYT PIA ACT172033, and Basal-CATA AFB170002 grants. A.K. gratefully acknowledges support from the YCAA Prize Postdoctoral Fellowship. E.G. acknowledges the generous support of the Cottrell College Award through the Research Corporation for Science Advancement.

Appendix

We show all the spectra in Figure A1 from SDSS with the relevant broad lines indicated. We discuss spectral fitting and derived quantities in a future paper (M. Estrada et al. 2020, in preparation).

Here we show the SED decomposition used to obtain $L_{\rm IR}$, SFR, and $f_{\rm AGN}$ in Figure A2. Each set of WISE and Herschel photometry is fit by a combination of the featureless AGN template from Kirkpatrick et al. (2012) and the submillimeter galaxy template from Pope et al. (2008). See details in Section 2.3.

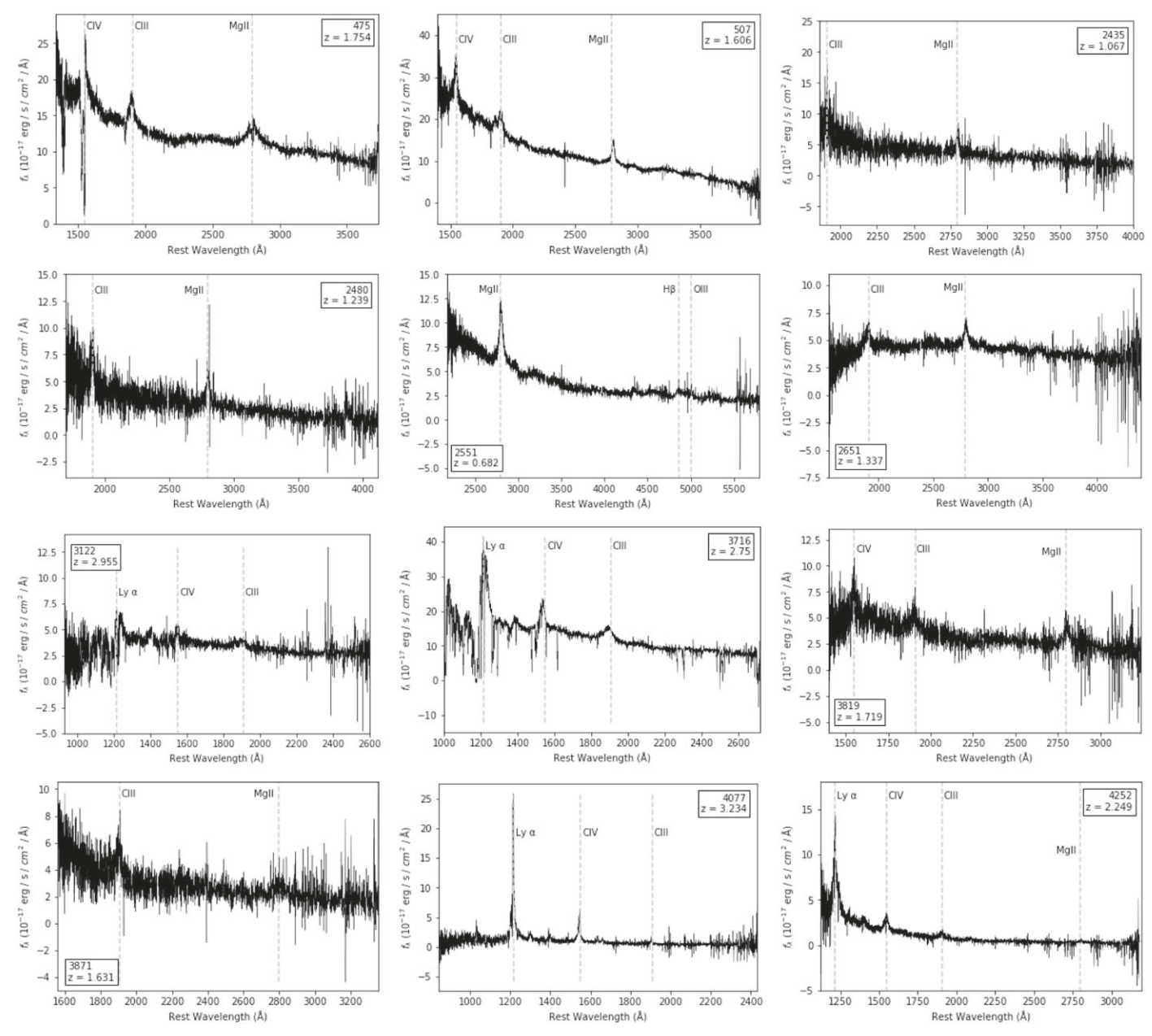


Figure A1. SDSS spectra of the cold quasars with the relevant lines marked.

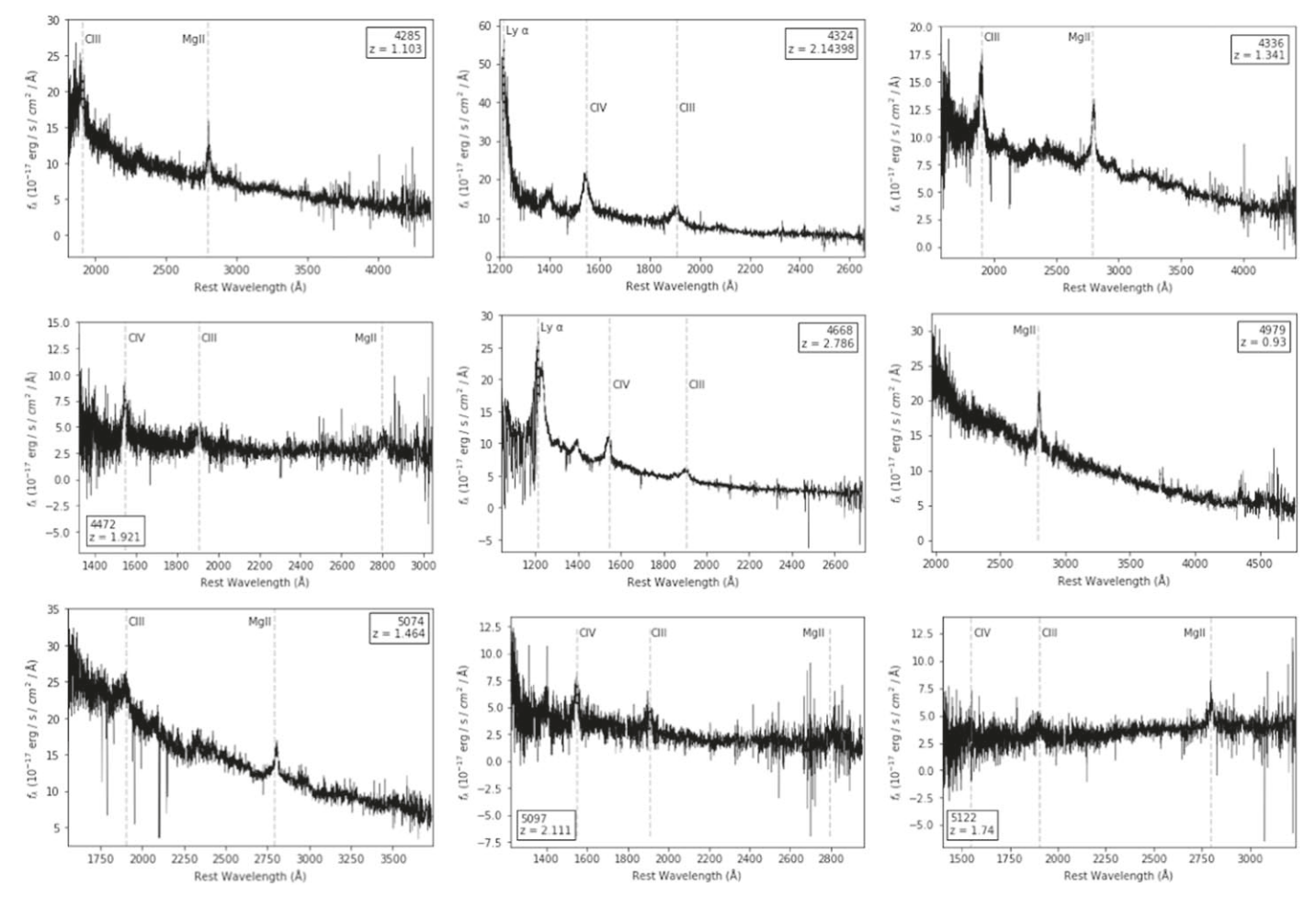


Figure A1. (Continued.)

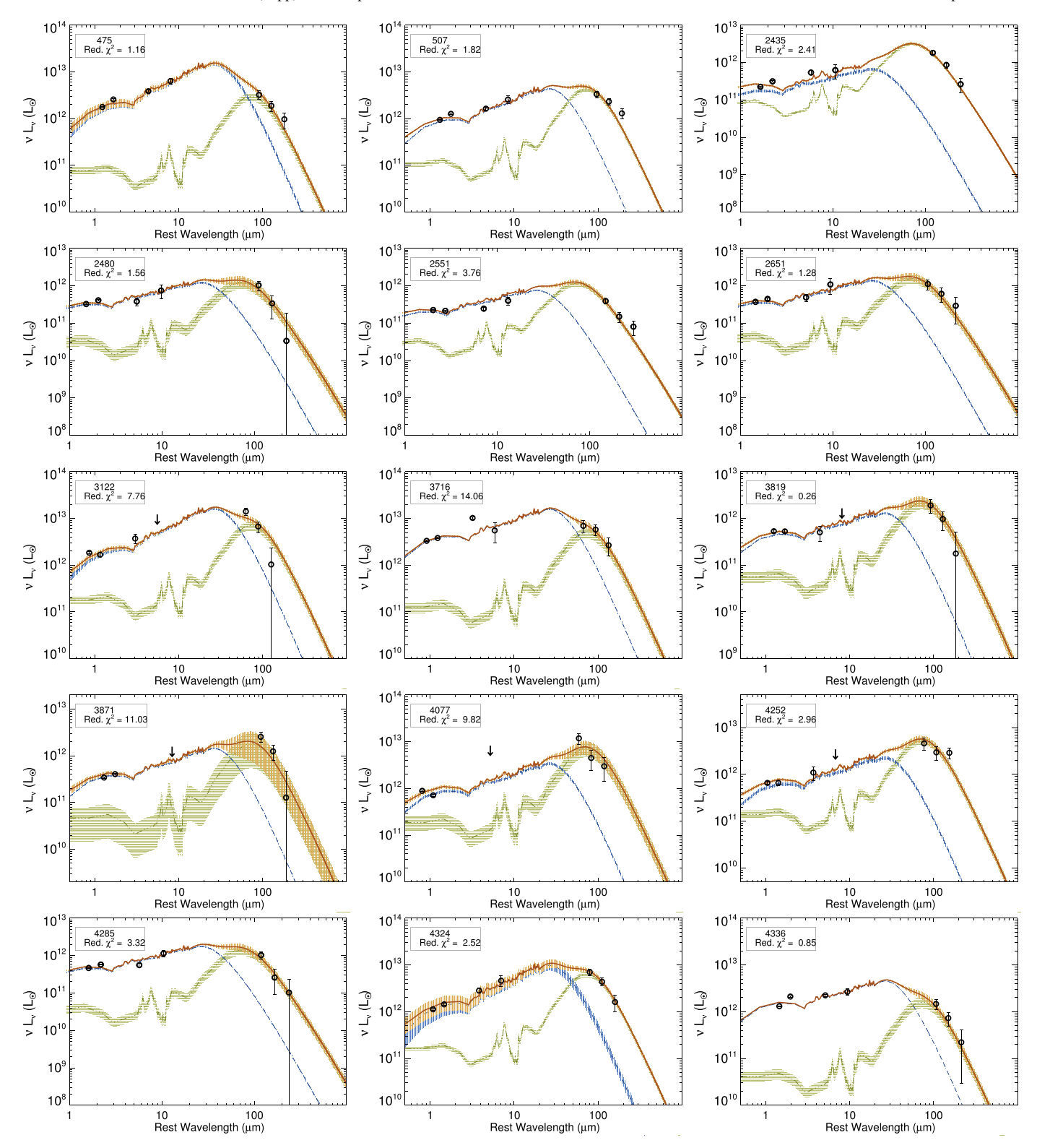


Figure A2. IR decomposition for all cold quasars. The black circles are the WISE and Herschel photometry, the orange line is the best-fit model, the blue line is the featureless AGN template, and the green line is host galaxy. The legend of each fit lists the reduced χ^2 .

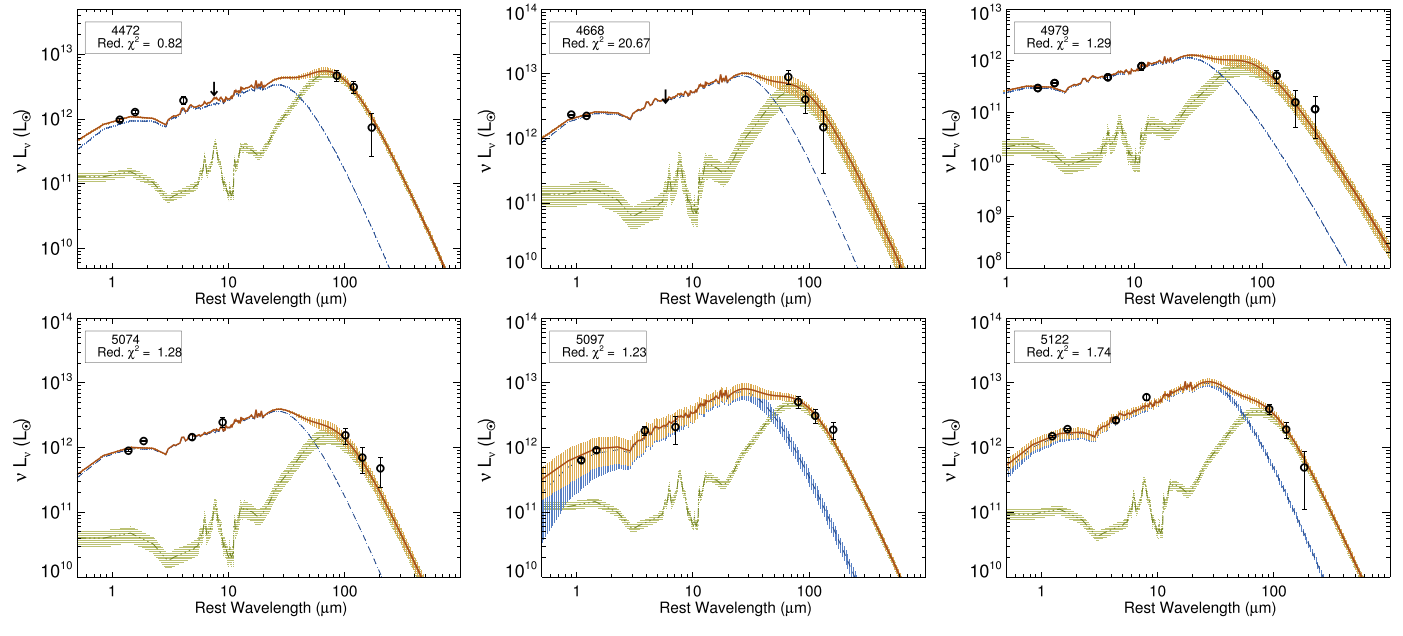


Figure A2. (Continued.)

ORCID iDs

Allison Kirkpatrick https://orcid.org/0000-0002-1306-1545 C. Megan Urry https://orcid.org/0000-0002-0745-9792 Kevin C. Cooke https://orcid.org/0000-0002-2200-9845 Eilat Glikman https://orcid.org/0000-0003-0489-3750 Tonima Tasnim Ananna https://orcid.org/0000-0001-Jeyhan S. Kartaltepe https://orcid.org/0000-0001-9187-3605

Stephanie M. LaMassa https://orcid.org/0000-0002-

5907-3330

Stefano Marchesi https://orcid.org/0000-0001-5544-0749 Meredith Powell https://orcid.org/0000-0003-2284-8603 Dave Sanders https://orcid.org/0000-0002-1233-9998 Ezequiel Treister https://orcid.org/0000-0001-7568-6412 Traceye Jan Turner https://orcid.org/0000-0003-2971-1722

References

```
Ananna, T. T., Salvato, M., LaMassa, S., et al. 2017, ApJ, 850, 66
Ananna, T. T., Treister, E., Urry, C. M., et al. 2019, ApJ, 871, 240
Arnouts, S., Cristiani, S., Moscardini, L., et al. 1999, MNRAS, 310, 540
Assef, R. J., Stern, D., Noirot, G., et al. 2018, ApJS, 234, 23
Azadi, M., Coil, A. L., Aird, J., et al. 2017, ApJ, 835, 27
Baldwin, J. A., Phillips, M. M., & Terlevich, R. 1981, PASP, 93, 5
Barvainis, R., & Ivison, R. 2002, ApJ, 571, 712
Bennert, V. N., Auger, M. W., Treu, T., Woo, J.-H., & Malkan, M. A. 2011,
     J, 742, 107
Berta, S., Lutz, D., Santini, P., et al. 2013, A&A, 551, A100
Boquien, M., Burgarella, D., Roehlly, Y., et al. 2019, A&A, 622, A103
Brandt, W. N., Alexander, D. M., Hornschemeier, A. E., et al. 2001, AJ,
Brightman, M., Nandra, K., Salvato, M., et al. 2014, MNRAS, 443, 1999
Buchner, J., & Bauer, F. E. 2017, MNRAS, 465, 4348
Buchner, J., Schulze, S., & Bauer, F. E. 2017, MNRAS, 464, 4545
Burgarella, D., Buat, V., & Iglesias-Páramo, J. 2005, MNRAS, 360, 1413
Cappelluti, N., Hasinger, G., Brusa, M., et al. 2007, ApJS, 172, 341
Casey, C. M., Narayanan, D., & Cooray, A. 2014, PhR, 541, 45
Ciotti, L., & Ostriker, J. P. 2007, ApJ, 665, 1038
Civano, F., Marchesi, S., Comastri, A., et al. 2016, ApJ, 819, 62
```

Coppin, K. E. K., Swinbank, A. M., Neri, R., et al. 2008, MNRAS, 389, 45

Conroy, C., & White, M. 2013, ApJ, 762, 70

```
Dai, Y. S., Elvis, M., Bergeron, J., et al. 2014, ApJ, 791, 113
Dey, A., Schlegel, D. J., Lang, D., et al. 2019, AJ, 157, 168
Donley, J. L., Koekemoer, A. M., Brusa, M., et al. 2012, ApJ, 748, 142
Draine, B. T. 2003, ARA&A, 41, 241
Eisenhardt, P. R. M., Wu, J., Tsai, C.-W., et al. 2012, ApJ, 755, 173
Elbaz, D., Daddi, E., le Borgne, D., et al. 2007, A&A, 468, 33
Elbaz, D., Dickinson, M., Hwang, H. S., et al. 2011, A&A, 533, A119
Elitzur, M., & Shlosman, I. 2006, ApJL, 648, L101
Elvis, M., Civano, F., Vignali, C., et al. 2009, ApJS, 184, 158
Elvis, M., Wilkes, B. J., McDowell, J. C., et al. 1994, ApJS, 95, 1
Flaugher, B., Diehl, H. T., Honscheid, K., et al. 2015, AJ, 150, 150
Fliri, J., & Trujillo, I. 2016, MNRAS, 456, 1359
Frayer, D. T., Ivison, R. J., Scoville, N. Z., et al. 1998, ApJL, 506, L7
Fritz, J., Franceschini, A., & Hatziminaoglou, E. 2006, MNRAS, 366, 767
Fu, H., Isbell, J., Casey, C. M., et al. 2017, ApJ, 844, 123
Geach, J. E., Smail, I., Moran, S. M., et al. 2011, ApJL, 730, L19
Giacconi, R., Zirm, A., Wang, J., et al. 2002, ApJS, 139, 369
Giavalisco, M., Ferguson, H. C., Koekemoer, A. M., et al. 2004, ApJL,
  600, L93
Glikman, E., Gregg, M. D., Lacy, M., et al. 2004, ApJ, 607, 60
Glikman, E., Lacy, M., LaMassa, S., et al. 2018, ApJ, 861, 37
Glikman, E., LaMassa, S., Piconcelli, E., Urry, M., & Lacy, M. 2017, ApJ,
Glikman, E., Simmons, B., Mailly, M., et al. 2015, ApJ, 806, 218
Glikman, E., Urrutia, T., Lacy, M., et al. 2012, ApJ, 757, 51
Glikman, E., Urrutia, T., Lacy, M., et al. 2013, ApJ, 778, 127
González-Martín, O., Masegosa, J., García-Bernete, I., et al. 2019, ApJ,
Goulding, A. D., Alexander, D. M., Bauer, F. E., et al. 2012, ApJ, 755, 5
Green, R. F., Schmidt, M., & Liebert, J. 1986, ApJS, 61, 305
Groves, B., Dopita, M., & Sutherland, R. 2006, A&A, 458, 405
Hainline, K. N., Hickox, R. C., Chen, C.-T., et al. 2016, ApJ, 823, 42
Hainline, K. N., Shapley, A. E., Greene, J. E., & Steidel, C. C. 2011, ApJ,
Hatziminaoglou, E., Hernán-Caballero, A., Feltre, A., & Piñol Ferrer, N. 2015,
    ApJ, 803, 110
Heckman, T. M., & Best, P. N. 2014, ARA&A, 52, 589
Hickox, R. C., Jones, C., Forman, W. R., et al. 2009, ApJ, 696, 891
Hodge, J. A., Smail, I., Walter, F., et al. 2019, ApJ, 876, 130
Hodge, J. A., Swinbank, A. M., Simpson, J. M., et al. 2016, ApJ, 833, 103
Hönig, S. F., & Kishimoto, M. 2010, A&A, 523, A27
Hopkins, P. F., Hernquist, L., Cox, T. J., & Kereš, D. 2008, ApJS, 175, 356
Hopkins, P. F., Richards, G. T., & Hernquist, L. 2007, ApJ, 654, 731
Hopkins, P. F., Somerville, R. S., Hernquist, L., et al. 2006, ApJ, 652, 864
Ilbert, O., Arnouts, S., McCracken, H. J., et al. 2006, A&A, 457, 841
Imanishi, M., Nakanishi, K., & Izumi, T. 2016, AJ, 152, 218
Ivison, R. J., Page, M. J., Cirasuolo, M., et al. 2019, MNRAS, 489, 427
```

```
Jester, S., Schneider, D. P., Richards, G. T., et al. 2005, AJ, 130, 873
Jiang, L., Fan, X., Bian, F., et al. 2014, ApJS, 213, 12
Kamenetzky, J., Rangwala, N., Glenn, J., Maloney, P. R., & Conley, A. 2016,
   ApJ, 829, 93
Kirkpatrick, A., Alberts, S., Pope, A., et al. 2017, ApJ, 849, 111
Kirkpatrick, A., Pope, A., Alexander, D. M., et al. 2012, ApJ, 759, 139
Kirkpatrick, A., Pope, A., Charmandaris, V., et al. 2013, ApJ, 763, 123
Kirkpatrick, A., Pope, A., Sajina, A., et al. 2015, ApJ, 814, 9
Kirkpatrick, A., Sharon, C., Keller, E., & Pope, A. 2019, ApJ, 879, 41
Kocevski, D. D., Brightman, M., Nandra, K., et al. 2015, ApJ, 814, 104
la Plante, P., & Trac, H. 2016, ApJ, 828, 90
Lacy, M., Storrie-Lombardi, L. J., Sajina, A., et al. 2004, ApJS, 154, 166
LaMassa, S. M., Cales, S., Moran, E. C., et al. 2015, ApJ, 800, 144
LaMassa, S. M., Glikman, E., Brusa, M., et al. 2017, ApJ, 847, 100
LaMassa, S. M., Urry, C. M., Cappelluti, N., et al. 2013a, MNRAS, 436, 3581
LaMassa, S. M., Urry, C. M., Cappelluti, N., et al. 2016, ApJ, 817, 172
LaMassa, S. M., Urry, C. M., Glikman, E., et al. 2013b, MNRAS, 432, 1351
Lawrence, A., Warren, S. J., Almaini, O., et al. 2007, MNRAS, 379, 1599
Lee, N., Sanders, D. B., Casey, C. M., et al. 2015, ApJ, 801, 80
Lusso, E., Comastri, A., Simmons, B. D., et al. 2012, MNRAS, 425, 623
Lutz, D., Maiolino, R., Spoon, H. W. W., & Moorwood, A. F. M. 2004, A&A,
Lyu, J., & Rieke, G. H. 2017, ApJ, 841, 76
Lyu, J., & Rieke, G. H. 2018, ApJ, 866, 92
Mahoro, A., Pović, M., & Nkundabakura, P. 2017, MNRAS, 471, 3226
Marchesi, S., Civano, F., Elvis, M., et al. 2016, ApJ, 817, 34
Mateos, S., Alonso-Herrero, A., Carrera, F. J., et al. 2012, MNRAS, 426, 3271
McDowell, J. C., Elvis, M., Wilkes, B. J., et al. 1989, ApJL, 345, L13
McMahon, R. G., Banerji, M., Gonzalez, E., et al. 2013, Msngr, 154, 35
Mor, R., Netzer, H., & Elitzur, M. 2009, ApJ, 705, 298
Mullaney, J. R., Alexander, D. M., Goulding, A. D., & Hickox, R. C. 2011,
           , 414, 1082
Murphy, E. J., Condon, J. J., Schinnerer, E., et al. 2011, ApJ, 737, 67
Murray, N., Quataert, E., & Thompson, T. A. 2005, ApJ, 618, 569
Netzer, H., Lutz, D., Schweitzer, M., et al. 2007, ApJ, 666, 806
Noeske, K. G., Weiner, B. J., Faber, S. M., et al. 2007, ApJL, 660, L43
Omont, A., Beelen, A., Bertoldi, F., et al. 2003, A&A, 398, 857
Page, M. J., Stevens, J. A., Ivison, R. J., & Carrera, F. J. 2004, ApJL, 611, L85
Papovich, C., Shipley, H. V., Mehrtens, N., et al. 2016, ApJS, 224, 28
Perna, M., Sargent, M. T., Brusa, M., et al. 2018, A&A, 619, A90
Petric, A. O., Armus, L., Howell, J., et al. 2011, ApJ, 730, 28
Pontzen, A., & Governato, F. 2012, MNRAS, 421, 3464
```

```
Pope, A., Chary, R.-R., Alexander, D. M., et al. 2008, ApJ, 675, 1171
Ricci, C., Assef, R. J., Stern, D., et al. 2017, ApJ, 835, 105
Richards, G. T., Lacy, M., Storrie-Lombardi, L. J., et al. 2006, ApJS, 166, 470
Rosario, D. J., Santini, P., Lutz, D., et al. 2012, A&A, 545, A45
Rujopakarn, W., Daddi, E., Rieke, G. H., et al. 2019, ApJ, 882, 107
Rujopakarn, W., Dunlop, J. S., Rieke, G. H., et al. 2016, ApJ, 833, 12
Sajina, A., Yan, L., Fadda, D., Dasyra, K., & Huynh, M. 2012, ApJ, 757, 13
Salomé, Q., Salomé, P., & Combes, F. 2015, A&A, 574, A34
Sanders, D. B., & Mirabel, I. F. 1996, ARA&A, 34, 749
Schmidt, M., & Green, R. F. 1983, ApJ, 269, 352
Schulze, A., Silverman, J. D., Daddi, E., et al. 2019, MNRAS, 488, 1180
Scoville, N., Aussel, H., Brusa, M., et al. 2007, ApJS, 172, 1
Shangguan, J., & Ho, L. C. 2019, ApJ, 873, 90
Shen, Y., Richards, G. T., Strauss, M. A., et al. 2011, ApJS, 194, 45
Siebenmorgen, R., Heymann, F., & Efstathiou, A. 2015, A&A, 583, A120
Simpson, J. M., Smail, I., Swinbank, A. M., et al. 2019, ApJ, 880, 43
Soltan, A. 1982, MNRAS, 200, 115
Speagle, J. S., Steinhardt, C. L., Capak, P. L., & Silverman, J. D. 2014, ApJS,
  214, 15
Spoon, H. W. W., Marshall, J. A., Houck, J. R., et al. 2007, ApJL, 654,
Stacey, G. J., Hailey-Dunsheath, S., Ferkinhoff, C., et al. 2010, ApJ, 724, 957
Stanley, F., Alexander, D. M., Harrison, C. M., et al. 2017, MNRAS,
  472, 2221
Stern, D. 2015, ApJ, 807, 129
Stern, D., Assef, R. J., Benford, D. J., et al. 2012, ApJ, 753, 30
Stern, D., Eisenhardt, P., Gorjian, V., et al. 2005, ApJ, 631, 163
Stierwalt, S., Armus, L., Surace, J. A., et al. 2013, ApJS, 206, 1
Symeonidis, M., Giblin, B. M., Page, M. J., et al. 2016, MNRAS, 459, 257
Teng, S. H., Rigby, J. R., Stern, D., et al. 2015, ApJ, 814, 56
Timlin, J. D., Ross, N. P., Richards, G. T., et al. 2016, ApJS, 225, 1
Treister, E., Schawinski, K., Urry, C. M., & Simmons, B. D. 2012, ApJL,
   758, L39
Treister, E., Urry, C. M., Chatzichristou, E., et al. 2004, ApJ, 616, 123
Urrutia, T., Lacy, M., & Becker, R. H. 2008, ApJ, 674, 80
Urry, C. M., & Padovani, P. 1995, PASP, 107, 803
Viero, M. P., Asboth, V., Roseboom, I. G., et al. 2014, ApJS, 210, 22
White, R. L., Becker, R. H., Helfand, D. J., & Gregg, M. D. 1997, ApJ,
  475, 479
Willott, C. J., Martínez-Sansigre, A., & Rawlings, S. 2007, AJ, 133, 564
Wu, J., Jun, H. D., Assef, R. J., et al. 2018, ApJ, 852, 96
Wu, J., Tsai, C.-W., Sayers, J., et al. 2012, ApJ, 756, 96
```